

# Blended Locally-Optimal Control Laws for Space Debris Removal in LEO Using a Solar Sail

Christian Bianchi[a,b,*], Lorenzo Niccolai[b], Giovanni Mengali[b], Matteo Ceriotti[a]

[a] *James Watt School of Engineering, University of Glasgow, Glasgow, United Kingdom*
[b] *Department of Civil and Industrial Engineering, University of Pisa, Pisa, Italy*

**Abstract**

This paper proposes a preliminary design for a space debris removal mission in low Earth orbit that makes use of a solar sail as a chaser satellite to reach, capture and de-orbit a debris object. The sail employs solar radiation pressure as the main source of thrust, and it is also subjected to the effects of the aerodynamic forces, the oblateness of the Earth, as well as the occurrence of eclipses. Locally-optimal laws are used to control the transfer with the aim of maximizing (or minimizing) the rate of change of a specific orbital element or a suitable linear combination of them, depending on the phase of the transfer. When blended control laws are used to target the debris, optimal weighing factors are derived through a genetic algorithm to assess the relative importance of each orbital element. Numerical simulations show the effectiveness of locally-optimal laws in driving the sail towards the target even in the presence of the aforementioned orbital perturbations. In a test-case scenario, the sail, departing from 600 km of altitude, is able to reach the debris' orbit at 1200 km of height in less than 200 days with good accuracy for a preliminary study.

*Keywords:* Solar sail, Space debris, Locally-optimal control laws

## 1. Introduction

The increasing number of space debris objects in low Earth orbit poses a threat to operative satellites and might soon lead to the overcrowding of this orbital slot that would result in a much higher risk of collisions [1]. Several strategies to remove these objects have been proposed and investigated in the literature, such as passive de-orbiting that exploits natural perturbations (e.g., aerodynamic forces, solar radiation pressure) and drag-augmentation devices [2, 3, 4, 5, 6, 7, 8].

On the other hand, active removal strategies usually involve the use of a chaser satellite that can capture the debris and de-orbit it. These techniques are needed for larger objects, for which a controlled re-entry might be necessary, or objects located at higher altitudes where natural perturbations have little or no effect [9, 10].

Active strategies might also be employed for multiple debris removal missions, where a single spacecraft can dispose of more debris objects, thus drastically reducing the cost of the mission [11, 12, 13].

Most of these proposed strategies make use of conventional propulsion systems such as chemical or electric thrusters, that would constrain the mission duration to the limited amount of propellant that can be carried on board. Besides, chemical propellants also represent a very high percentage of the spacecraft mass, which results in a much higher cost of the launch.

The use of propellantless propulsion systems, such as solar sails, might represent a viable option for space debris removal missions around the Earth. Kelly and Bevilacqua [14, 15] analyzed minimum-time solar sail transfers to remove debris in geostationary orbit where the effect of the aerodynamic forces is negligible.

The aim of this paper is to investigate a single debris removal strategy in LEO that makes use of a solar sail to reach the debris' orbit, capture the object, and bring it down to a lower altitude where it can re-enter and burn into the atmosphere thanks to the aerodynamic forces. The advantage of using a solar sail lies in the fact that no propellant must be carried on board, which drastically reduces the spacecraft mass and the cost of launch.

In addition to the effect of the solar radiation pressure as the main source of thrust, the dynamical model used in this work considers also the natural perturbations present in low Earth orbits, such as the aerodynamic forces and the gravitational perturbation caused by the oblateness of the Earth. The presence of eclipses

*Corresponding author, christian.bianchi@phd.unipi.it

is also considered assuming that the Earth casts a cylindrical shadow.

The manuscript is organized as follows. Section 2 describes in detail the dynamical model used in this study, the equations of motion to propagate the sail trajectory, and all the perturbing accelerations acting on the spacecraft. In Section 3, the transfer model is introduced, and each phase is thoroughly described, together with the locally-optimal control laws used to optimize the trajectory. The results of the numerical simulations are shown and analyzed in Section 4 for each phase of the transfer. Finally, Section 5 draws the conclusions of this work and lays the foundations for further developments.

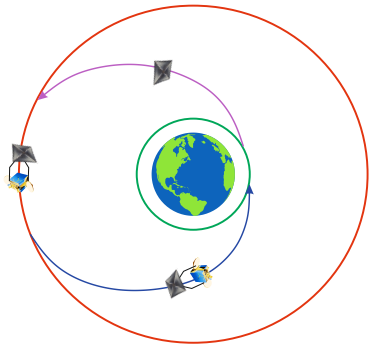

Figure 1: Simple scheme of the mission scenario. The sail departs from a circular parking orbit (green) to reach the target's orbit (red). After phasing, rendezvous and capture of the debris, the sail brings it down to a lower altitude.

## 2. Dynamical model

The dynamical model used in this work takes into account the presence of orbital perturbations such as the oblateness of the Earth through the $J_2$ coefficient, the atmospheric drag and lift acting upon the sail, as well as the solar radiation pressure (SRP) as the main source of thrust. To avoid singularities in presence of circular orbits, the spacecraft dynamics is described by means of a set of modified equinoctial orbital elements (MEOEs) [16, 17]

$$\begin{aligned} p &= a\,(1-e^2) \\ f &= e\,\cos\left(\Omega+\omega\right), \quad g = e\,\sin\left(\Omega+\omega\right) \\ h &= \tan\left(i/2\right)\,\cos\left(\Omega\right), \quad k = \tan\left(i/2\right)\,\sin\left(\Omega\right) \\ L &= \Omega+\omega+\nu \end{aligned} \tag{1}$$

The equations of motion in terms of MEOEs can be written in vector form as [18]

$$\dot{\boldsymbol{x}} = \mathbb{A}(\boldsymbol{x})\,\boldsymbol{a} + \boldsymbol{b}(\boldsymbol{x}) \tag{2}$$

where $\boldsymbol{x} = [p,\ f,\ g,\ h,\ k,\ L]^{\mathrm{T}}$ is the spacecraft state vector.

The coefficients of the matrix $\mathbb{A} \in \mathbb{R}^{6\times 6}$ are

$$\begin{aligned} A_{1,2} &= \frac{2p}{q}\sqrt{\frac{p}{\mu}}, \quad A_{2,1} = \sqrt{\frac{p}{\mu}}\sin L \\ A_{2,2} &= \sqrt{\frac{p}{\mu}}\frac{1}{q}\{(q+1)\cos L + f\} \\ A_{2,3} &= -\sqrt{\frac{p}{\mu}}\frac{g}{q}\{h\sin L - k\cos L\} \\ A_{3,1} &= -\sqrt{\frac{p}{\mu}}\cos L \\ A_{3,2} &= \sqrt{\frac{p}{\mu}}\frac{1}{q}\{(q+1)\sin L + g\} \\ A_{3,3} &= \sqrt{\frac{p}{\mu}}\frac{f}{q}\{h\sin L - k\cos L\} \\ A_{4,3} &= \sqrt{\frac{p}{\mu}}\frac{s^2\cos L}{2q}, \quad A_{5,3} = \sqrt{\frac{p}{\mu}}\frac{s^2\sin L}{2q} \\ A_{6,3} &= \sqrt{\frac{p}{\mu}}\frac{1}{q}\{h\sin L - k\cos L\} \end{aligned} \tag{3}$$

while the remaining ones are all zero.

The vector $\boldsymbol{b}$ is simply

$$\boldsymbol{b} = \begin{bmatrix} 0 & 0 & 0 & 0 & 0 & \sqrt{\mu p}\left(\frac{q}{p}\right)^2 \end{bmatrix}^{\mathrm{T}} \tag{4}$$

where $q = 1 + f\cos L + g\sin L$ and $s^2 = 1 + h^2 + k^2$.

The term $\boldsymbol{a}$ is the vector of perturbing accelerations expressed in the Radial-Transversal-Normal (RTN) reference frame $\mathcal{T}_{\mathrm{RTN}}$, whose different contributions are explained in detail in the following subsections.

### 2.1. Solar radiation pressure

In this study, an ideal force model is used to express the thrust generated by the solar sail [19], which is therefore assumed to be a flat and perfectly reflecting surface, able to generate a propulsive acceleration given by

$$\boldsymbol{a}_{\mathrm{SRP}} = \eta\, a_c\, \cos^2\alpha\, \hat{\boldsymbol{n}} \tag{5}$$

where $\eta = \{0, 1\}$ is the shadow factor that models the occurrence of eclipses, $a_c$ is the sail characteristic acceleration, $\hat{\boldsymbol{n}}$ is the unit vector perpendicular to the sail plane, and $\alpha \in [0,\ \pi/2]$ is the sail cone angle between $\hat{\boldsymbol{n}}$ and the Sun-sail direction. In this work, the dependence of the SRP on the distance from the Sun is neglected due to the small eccentricity of Earth's orbit. In accordance with Carzana et al. [20], introduce a sail-centered Sun-light reference frame $\mathcal{T}_S$, whose $\hat{\boldsymbol{x}}_S$ axis coincides with

the instantaneous Sun-sail vector, $\hat{\boldsymbol{y}}_{\mathrm{S}} = \hat{\boldsymbol{z}}_{\mathrm{I}} \times \hat{\boldsymbol{x}}_{\mathrm{S}}$ (where $\hat{\boldsymbol{z}}_{\mathrm{I}}$ is the third axis of a Geocentric-Equatorial reference frame) and $\hat{\boldsymbol{z}}_{\mathrm{S}}$ completes the right-handed frame (see Fig. 2). The unit vector $\hat{\boldsymbol{n}}$ expressed in the Sunlight reference frame $\mathcal{T}_S$ is

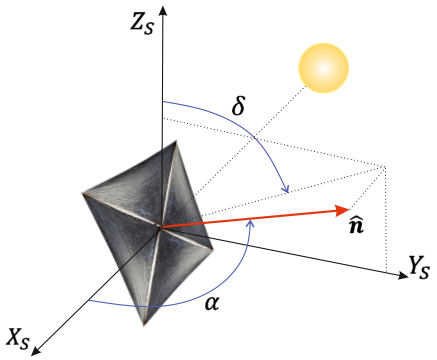


Figure 2: Cone ($\alpha \in [0, \pi/2]$) and clock ($\delta \in [0, 2\pi]$) angles that define the orientation of the sail normal unit vector $\hat{\boldsymbol{n}}$ with respect to the Sunlight reference frame $\mathcal{T}_S$.

$$[\hat{\boldsymbol{n}}]_{\mathrm{S}} = [\cos\alpha \quad \sin\alpha\,\sin\delta \quad \sin\alpha\,\cos\delta]^{\mathrm{T}} \tag{6}$$

which must be transformed into the RTN reference frame $\mathcal{T}_{\mathrm{RTN}}$ by means of the transformation matrix $\mathbb{R}_{\mathrm{S}\to\mathrm{RTN}}$ which depends on the sail state and the Sun's position.

### 2.2. Atmospheric drag and lift

When the sail orbits through the Earth's atmosphere, it experiences aerodynamics forces (drag and lift) that can be modelled assuming the sail to be a flat plate. Moreover, in agreement with Refs. [20, 21], a hyperthermal free-molecular flow is considered, which means that the spacecraft velocity is much larger than the thermal velocity of the atmospheric particles [22].

Under these assumptions, the drag and lift accelerations can be expressed as

$$\boldsymbol{a}_{\mathrm{D}} = -\frac{1}{2}\frac{\rho v^2}{\sigma} C_D\, \hat{\boldsymbol{v}} \tag{7}$$

$$\boldsymbol{a}_{\mathrm{L}} = \frac{1}{2}\frac{\rho v^2}{\sigma} C_L\, \hat{\boldsymbol{L}} \tag{8}$$

where $\rho$ is the atmospheric density provided by the MATLAB built-in function *atmosnrlmsise00* based on the NRLMSISE-00 model [23], $v$ and $\hat{\boldsymbol{v}}$ are the sail velocity magnitude and direction, respectively, and $\sigma$ is the sail loading, defined as the ratio of the total mass to the sail area. The unit vector $\hat{\boldsymbol{L}}$, which identifies the lift orientation, can be computed as [24]

$$\hat{\boldsymbol{L}} = \mathrm{sign}\left(\hat{\boldsymbol{v}} \cdot \hat{\boldsymbol{n}}\right) \frac{\hat{\boldsymbol{v}} \times (\hat{\boldsymbol{v}} \times \hat{\boldsymbol{n}})}{\|\hat{\boldsymbol{v}} \times \hat{\boldsymbol{n}}\|} \tag{9}$$

The drag and lift coefficients $C_D$ and $C_L$ are defined as

$$C_D = 2\left[\sigma_T + \sigma_N V_R\,|\cos\zeta| + (2 - \sigma_N - \sigma_t)\cos^2\zeta\right]|\cos\zeta| \tag{10}$$

$$C_L = 2\left[\sigma_N V_R + (2 - \sigma_N - \sigma_T)\cos^2\zeta\right]|\cos\zeta|\,\sin\zeta \tag{11}$$

where $\zeta \in [0, \pi]$ is the angle between the sail normal vector $\hat{\boldsymbol{n}}$ and the spacecraft velocity $\hat{\boldsymbol{v}}$, $\sigma_N$ and $\sigma_T$ are the normal and tangential accommodation coefficients, and $V_R$ is the ratio of the average particle thermal speed to the spacecraft velocity. Typical values for these coefficient can be found in the literature [20, 21] to be $\sigma_N = \sigma_T = 0.8$, $V_R = 0.05$.

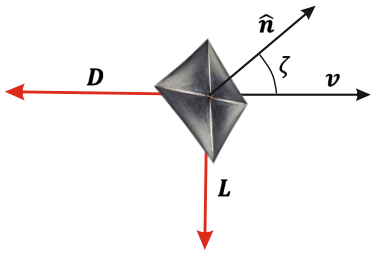


Figure 3: Orientation of drag $\boldsymbol{D}$ and lift $\boldsymbol{L}$ vectors. Also shown is the angle $\zeta$ between the velocity vector $\boldsymbol{v}$ and the sail unit vector $\hat{\boldsymbol{n}}$.

### 2.3. Earth's oblateness

The non-spherical gravitational field of the Earth is modelled by means of the $J_2$ harmonic coefficient, and the perturbing acceleration in the RTN reference frame can be expressed in terms of MEOEs as

$$[\boldsymbol{a}_{J_2}]_{\mathrm{R}} = -\frac{3\mu J_2 R_\oplus^2}{2r^4}\left[1 - \frac{12\,(h\sin L - k\cos L)^2}{(1 + h^2 + k^2)^2}\right]$$

$$[\boldsymbol{a}_{J_2}]_{\mathrm{T}} = -\frac{12\mu J_2 R_\oplus^2}{r^4}\left[\frac{(h\sin L - k\cos L)\,(h\cos L + k\sin L)}{(1 + h^2 + k^2)^2}\right]$$

$$[\boldsymbol{a}_{J_2}]_{\mathrm{N}} = -\frac{6\mu J_2 R_\oplus^2}{r^4}\left[\frac{(1 - h^2 - k^2)\,(h\sin L - k\cos L)}{(1 + h^2 + k^2)^2}\right] \tag{12}$$

where $R_\oplus = 6378.14\,\mathrm{km}$ is the mean equatorial radius of the Earth and $J_2 = 1.082\,626\,925\,639 \times 10^{-3}$ is the Earth's second harmonic coefficient.

### 2.4. Eclipses

The occurrence of eclipses is taken into account in this paper by means of a cylindrical model (see Fig. 4), which only distinguishes between sunlit phases (shadow factor $\eta = 1$) and shadow ($\eta = 0$). At the beginning of each propagation arc, the sail and Sun positions with respect to the Earth are used to verify whether the sail is in eclipse or not by means of the geometrical approach described in Ref. [25].

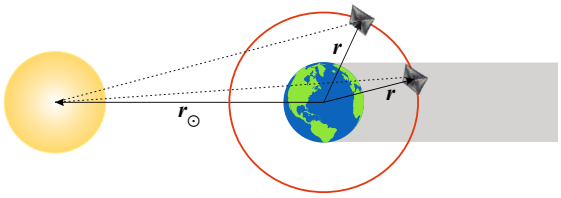


Figure 4: Cylindrical model used for eclipses.

## 3. Transfer Strategy

This section describes the transfer strategy to reach the debris' orbit starting from a lower altitude parking orbit which is assumed to be circular and at the same inclination as the one of the target debris. This assumption is consistent with a population of debris objects spread on circular orbits at a different right ascensions at the same inclination.

Due to the complex dynamics in a highly-perturbed environment, locally-optimal control laws have been employed to optimize the sail trajectory [26, 27]. The aim of these laws is to maximize (or minimize) the rate of change of an osculating orbital element as given by Gauss' form of the Lagrange planetary equations [25]. When the perturbing accelerations are small enough, these laws have been proven to be a good approximation to minimum-time transfers, especially in a preliminary mission design. Besides, several works have shown the possibility of blending these laws in order to control more orbital elements at the same time [26, 28].

The first part of the mission consists in reaching the debris' orbit starting from a lower altitude parking orbit, and it has been divided into two phases as shown in Fig. 5. In the 1st leg, the sail is controlled in such a way to increase its semimajor axis as quickly as possible to get away from the densest layers of the atmosphere. This phase ends as soon as the sail's osculating orbit reaches a perigee altitude $h_P = 1000$ km. This threshold has been chosen *a priori* as a height where the atmospheric density becomes almost negligible, but it might be possible to optimize it in a future work.

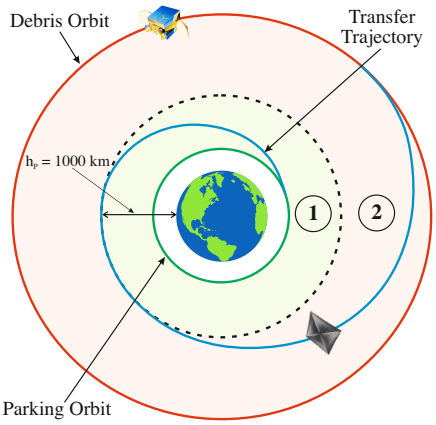


Figure 5: Transfer strategy to reach the debris' orbit (red) starting from a circular parking orbit at a lower altitude (green). The ascending part is divided into two phases, which are thoroughly described in Subsections 3.1-3.2.

During the 1st phase, only the semimajor axis is actively controlled, while the other orbital parameters are free, meaning that a 2nd phase is needed in order to drive all the four orbital elements of interest (i.e., $a, e, i, \Omega$) to match those of the target at the end of the transfer. It must be observed that, as we are dealing with transfers between circular orbits, the argument of perigee $\omega$ is meaningless.

Once the sail has reached the debris' orbit, it will perform phasing maneuvers, rendezvous and capture, before starting the descent phase at the end of which the debris is brought down to a lower altitude and released to re-enter into the atmosphere.

### 3.1. 1st Phase: semimajor axis increase

As previously stated, the aim of the 1st phase is to increase the semimajor axis of the sail's orbit as quickly as possible. This can be achieved by looking for the sail attitude that maximizes the time derivative of the semimajor axis at each time instant, that is

$$\max_{\{\alpha,\delta\}} \frac{da}{dt} \tag{13}$$

where $da/dt$ is given by the corresponding Lagrange's planetary equation

$$\frac{da}{dt} = 2\sqrt{\frac{a^3}{\mu\,(1-e^2)}}\left[e\,\sin\nu\,a_R + (1+e\,\cos\nu)\,a_T\right] \tag{14}$$

This amounts to maximizing the component of the thrust along the velocity vector [21].

The transfer has been divided into short-duration arcs of a few minutes each. At the beginning of each arc, the

Sun and sail positions are computed, as well as the local atmospheric density. The optimal sail attitude is then derived and maintained constant during the propagation along that arc. The simulation is stopped as soon as the osculating perigee altitude reaches 1000 km.

### 3.2. 2nd Phase: debris targeting

In this phase, it is necessary to control more orbital elements at the same time in order to reach the target's orbit at the end of the transfer. As already mentioned, the actual phasing between the sail and the debris is neglected in this work, and thus the true anomaly $\nu$ is not actively controlled. Besides, as the transfer takes place between circular orbits, also the argument of perigee $\omega$ is meaningless. Of the four remaining parameters, it must be observed that three of them (i.e., $a, e, i$) undergo only zero-averaged fluctuations due to the $J_2$ effect. On the other hand, the right ascension of the ascending node $\Omega$ has a well-known secular drift (negative for prograde orbits) of up to a few degrees per day, depending on the characteristics of the orbit. As the SRP thrust is extremely small, its effect on $\Omega$ is negligible if compared to the aforementioned secular drift. For this reason, the right ascension is not included in the solar sail's control law, but the need of phasing it with the target sets the duration of the transfer.

To this aim, a simple approach has been used to estimate the flight time of the 2nd phase, based on the constraint that, at the end of the transfer, the right ascension of the sail $\Omega$ must match the one of the target (indicated as $\Omega_t$ from now on). Starting from the sail state at the beginning of the 2nd leg $\{a_0, e_0, i_0, \Omega_0\}$ (which coincides with the state at the end of the 1st phase) and knowing the characteristics of the target's orbit $\{a_t, e_t, i_t\}$, an averaged linear drift is assumed for the sail's right ascension, that is

$$\dot{\Omega}_{\text{avg}} = -\frac{3}{2} \frac{J_2 \sqrt{\mu} R_\oplus^2}{a_{\text{avg}}^{7/2} (1 - e_{\text{avg}}^2)^2} \cos i_{\text{avg}} \tag{15}$$

where

$$a_{\text{avg}} = \frac{a_0 + a_t}{2}, \quad e_{\text{avg}} = \frac{e_0 + e_t}{2}, \quad i_{\text{avg}} = \frac{i_0 + i_t}{2} \tag{16}$$

Given this assumption, the RAAN of the sail and of the debris both decrease linearly according to

$$\Omega(t) = \Omega_0 + \dot{\Omega}_{\text{avg}}\, t \tag{17}$$

$$\Omega_t(t) = \Omega_{t,0} + \dot{\Omega}_t\, t \tag{18}$$

The flight time $\Delta t$ is therefore given by the condition $\Omega(\Delta t) = \Omega_t(\Delta t)$ (see Fig. 6).

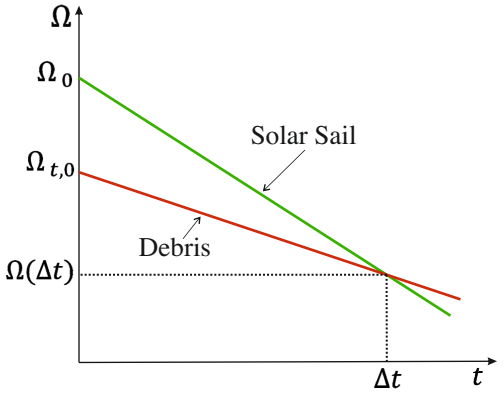


Figure 6: Flight time $\Delta t$ of the 2nd phase derived from the RAAN matching condition.

The remaining three orbital elements (i.e., $a, e, i$) are actively controlled by a suitable blending of the corresponding time derivatives which are

$$\frac{de}{dt} = \sqrt{\frac{a(1-e^2)}{\mu}} \left[ \sin\nu\, a_R + \left( \cos\nu + \frac{e + \cos\nu}{1 + e\cos\nu} \right) a_T \right] \tag{19}$$

$$\frac{di}{dt} = \sqrt{\frac{a(1-e^2)}{\mu}} \frac{\cos(\omega + \nu)}{1 + e\cos\nu}\, a_N \tag{20}$$

together with Eq. (14). The objective function $J$ to locally-optimize has been written as a linear combination of these time derivatives, such as

$$J = W_a R_a \frac{d(a/a_0)}{dt} + W_e R_e \frac{de}{dt} + W_i R_i \frac{di}{dt} \tag{21}$$

where $\{W_a, W_e, W_i\}$ are constant weights that express the relative importance of each orbital element, and $\{R_a, R_e, R_i\}$ are variable weights that depend on the "distance" from the target's orbit [29], that is

$$R_a = \frac{a - a_t}{|a_0 - a_t|}, \quad R_e = \frac{e - e_t}{|e_0 - e_t|}, \quad R_i = \frac{i - i_t}{|i_0 - i_t|} \tag{22}$$

The optimal sail attitude $\{\alpha_{\text{opt}}, \delta_{\text{opt}}\}$ is computed as the one that minimizes the objective function $J$ at each time. The role of these weights is to adjust the relative importance of each orbital element as the sail approaches the target and prioritize the one that is furthest from the target. As a matter of fact, these weights tend to zero as the corresponding element tends to the target value. Moreover, the numerators provide the sign of the weight, which indicates whether the corresponding time derivative has to be maximized or minimized.

The constant weights can be chosen in the range $[0, 1]$ without loss of generality, and must be selected in such

a way that the sail reaches the target after a flight time set by the RAAN matching condition. To do so, a genetic algorithm has been set up with the objective of minimizing the function

$$F = \left(\frac{a_{\text{fin}} - a_t}{a_0}\right)^2 + (e_{\text{fin}} - e_t)^2 + (i_{\text{fin}} - i_t)^2 + (\Omega_{\text{fin}} - \Omega_{t,\text{fin}})^2 \tag{23}$$

As the time to simulate a single transfer was long and computationally expensive, an approximate model has to be employed to run the genetic algorithm. As shown in Fig. 7, the first step in the approximate model consists in computing the keplerian orbital period $T_1$ at the current semimajor axis $a_1$ according to Kepler's third law. The local optimization and propagation is then carried out for a time equal to the orbital period and the difference $\Delta oe_1$ between the final and the initial orbital elements is evaluated. At this point, the model assumes a linear evolution of all the orbital elements for a time interval equal to $N$ times the orbital period $T_1$. After the time $NT_1$, the value of each orbital element is simply computed as $oe(NT_1) = oe(0) + N\,\Delta oe_1$. The same procedure is repeated $M$ times, where $M$ is given by the total flight time derived by the RAAN matching condition described in Subsec. 3.2. On the other hand, the value of $N$ is a trade-off choice between a more accurate approximation (smaller $N$) and a shorter computational time (greater $N$). In the numerical simulations described in Subsec. 4.2, a value $N = 30$ is used.

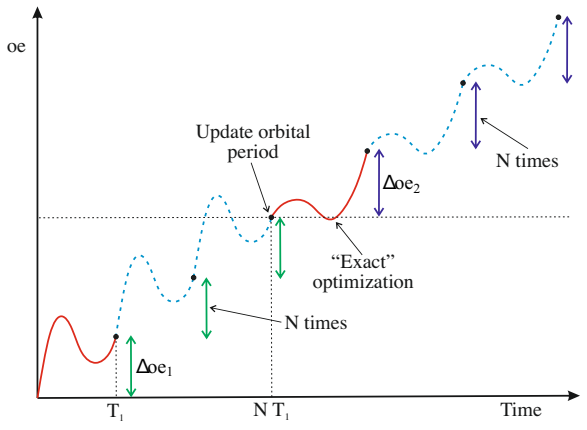


Figure 7: Approximate model for the 2nd phase transfer used to reduce the computational time of the genetic algorithm.

### 3.3. Descent Phase

After capturing the debris, the sail has to bring it down to a lower altitude and release it. In this descent phase, the sail departs from the debris' orbit and targets the initial circular parking orbit at a lower altitude, but at the same inclination. Obviously, no RAAN matching is needed in this phase and the flight time is left free. The only parameters of interest to be actively controlled are the semimajor axis $a$, the eccentricity $e$ and the inclination $i$. It must be pointed out that the additional mass of the captured debris has to be considered, resulting in a higher sail loading $\sigma_{\text{desc}} > \sigma$ and a lower characteristic acceleration $a_{c,\text{desc}} < a_c$.

A blended control law similar to the one in Eq. (21) has been used, that is

$$J = R_a \frac{d(a/a_0)}{dt} + R_e \frac{de}{dt} + R_i \frac{di}{dt} \tag{24}$$

where the variable weights are now defined as

$$R_a = \frac{a - a_t}{|a_0 - a_t|}, \quad R_e = e - e_t, \quad R_i = i - i_t \tag{25}$$

since the initial and final orbits have now the same eccentricity and inclination, and therefore some denominators in Eq. (22) would be equal to zero. As the flight time is not constrained, there is no need to include and optimize the constant weights, but the trajectory is propagated until the sail reaches the disposal orbit within a certain tolerance.

## 4. Numerical Simulations

In this Section, the transfer strategy described in Sec. 3 is applied to a test-case scenario using a solar sail with characteristic acceleration $a_c = 0.1\,\text{mm/s}^2$, that departs from a circular parking orbit at an altitude $h_0 = 600\,\text{km}$ above the Earth and initial right ascension $\Omega_0 = 0\,\text{deg}$. The departure date is the 1st January 2030, when the solar activity is close to a minimum.

### 4.1. 1st Phase: numerical results

The results obtained for the 1st phase of the transfer are shown in Fig. 8. In this case, the sail has reached the threshold perigee altitude $h_P = 1000\,\text{km}$ after about 92 days, showing an increase in the semimajor axis of roughly 450 km, which is compatible with similar analyses carried out in the literature [20]. The three orbital elements $\{a, e, i\}$ clearly show the fluctuations due to the J2 effect, which is also responsible for the evident secular drift in the right ascension $\Omega$.

### 4.2. 2nd Phase: numerical results

The 2nd phase of the transfer consists in targeting the debris' orbit using the blended control law defined in Eq. (21). As explained in Subsec. 3.2, the flight time

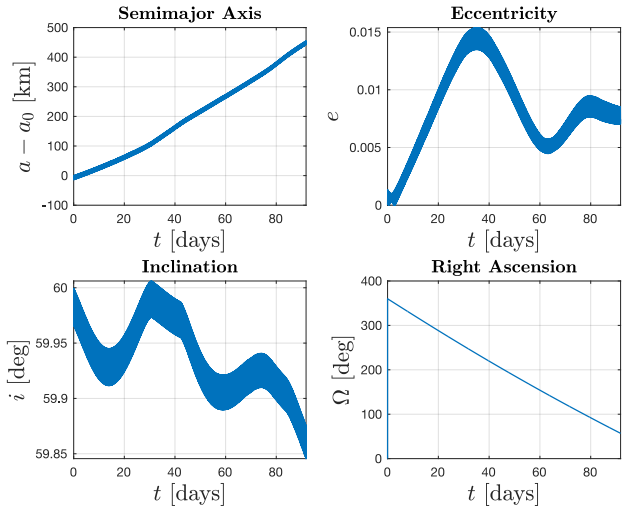


Figure 8: Evolution of the four orbital elements of interest $\{a, e, i, \Omega\}$ during the 1st phase of the transfer for a solar sail with characteristic acceleration $a_c = 0.1\,\mathrm{mm/s^2}$.

is fixed and provided by the RAAN matching condition. As a test-case scenario, an initial RAAN difference $\Delta\Omega_0 = 10\,\mathrm{deg}$ between the sail and the debris has been assumed, which lead to a flight time of approximately 101.9 days. It is worth pointing out that, if the initial RAAN difference is too small, the flight time would be shorter as well, and it might be impossible to drive some orbital elements towards the target in such a short time. On the other hand, longer flight times drastically increase the computational time for the genetic algorithm.

Given the flight time, a genetic algorithm is run with the approximate model to find the optimal values of the constant weights $\{W_a, W_e, W_i\}$. These values have been then used to propagate the trajectory both with the approximate and with the "exact" model.

The settings of the genetic algorithm and the optimal weights are shown in Tab. 1. Despite the low number of generations used in this simulation, the results plotted in Fig. 9 show that all the orbital elements are effectively driven towards their target values.

Table 2 shows the final values of the sail orbital elements obtained with both the approximate and the "exact" model. The final error in the semimajor axis obtained with the more accurate propagation is less than 4 km, the final eccentricity is about $1.7 \times 10^{-3}$, and the inclination seems to match very well the target value. These results are considered to be acceptable in a preliminary study, and are expected to improve if the genetic algorithm has time to better explore the solution space.

A comment is needed on the final right ascension, which, despite being very close to the target according to the approximate model, it actually shows a 2.84 deg discrepancy when the "exact" model is used. This error is due to the fact that it is sometimes difficult to precisely match the desired flight time with the approximate model, as the shortest time interval is made of $N = 30$ cycles which correspond to more than 2 days. This time step is then multiplied for an integer number $M$, which might lead to a little discrepancy between the flight time imposed by the RAAN matching condition (and used to propagate the exact model) and the one used in the approximate model. Despite this difference being relatively small, the right ascension has a drift of about 3 deg per day on that orbit, thus leading to the observed error in the final value. A possible solution to this issue might be to reduce the number of cycles $N$, but this would also lead to a much longer computational time.

Table 1: Genetic algorithm settings, flight time and optimal weights for the 2nd phase of the transfer.

| | |
|---|---|
| Population Size | 50 |
| Elite Count | 2 |
| Generations | 10 |
| Function Tol | $1 \times 10^{-6}$ |
| Flight Time $\Delta t$ | 101.9 days |
| $W_a$ | 0.27849822 |
| $W_e$ | 0.83082863 |
| $W_i$ | 0.76324954 |

Table 2: Numerical results of the 2nd phase. Both the approximate and the "exact" models are propagated using the weights obtained from the genetic algorithm.

| Orbit | $a$ [km] | $e$ | $i$ [deg] | $\Omega$ [deg] |
|---|---|---|---|---|
| Sail initial | 7433.5 | 0.0074 | 59.87 | 56.98 |
| Debris initial | 7578.1 | 0 | 60 | 46.98 |
| Debris final | | | | 130.07 |
| Sail (approx.) | 7588.7 | 0.0009 | 59.99 | 130.05 |
| Sail ("exact") | 7574.4 | 0.0017 | 60 | 127.23 |

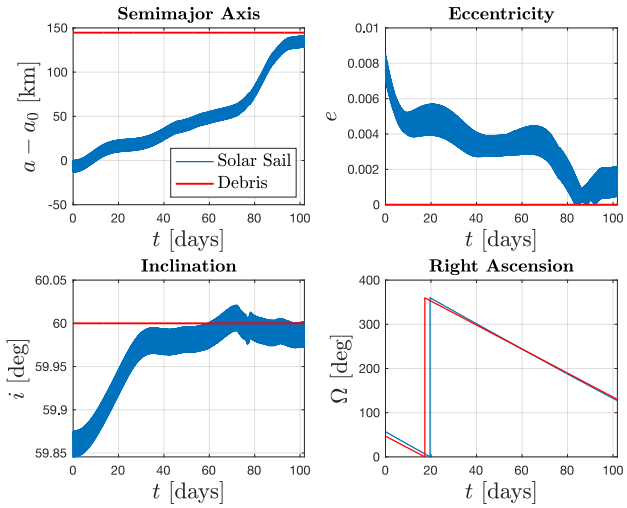


Figure 9: Evolution of the orbital elements in the 2nd phase of the transfer.

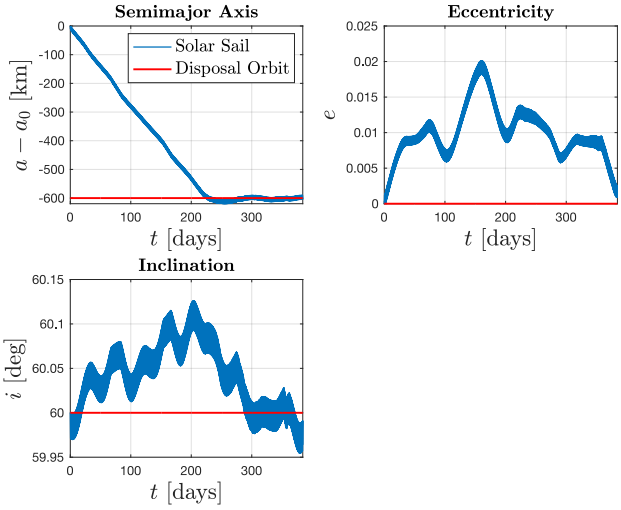


Figure 10: Evolution of the three orbital elements $\{a, e, i\}$ (blue) during the descent phase after capturing the debris. The red lines indicate the orbital elements of the target orbit, which coincides with the initial parking orbit.

### *4.3. Descent: numerical results*

The last phase of the mission is the descent to bring the debris down to the initial sail parking orbit and release it where the aerodynamic forces can lead to its atmospheric re-entry. The additional mass of the debris is taken into account by doubling the sail loading $\sigma_{\text{desc}} = 2\sigma$, which means that the new characteristic acceleration of the sail is $a_{c,\text{desc}} = a_c/2 = 0.05\,\text{mm/s}^2$. The simulation is started roughly 45 days after the end of the 2nd phase, to allow for phasing maneuvers, rendezvous and capture. The simulation has been propagated for 400 days, and the minimum value of the function $D = ((a-a_t)/a_0)^2 + (e-e_t)^2 + (i-i_t)^2$ has been used as a stopping criterion to generate the plots in Fig. 10. With this approach, the descent phase lasts about 384 days, but it must be observed that both the semimajor axis and the inclination have reached the target values after around 300 days. The residual small eccentricity after that time might be negligible if no particularly accurate orbit is required for the debris disposal.

A possible improvement to this approach would be to include some constant weights in the blended control law in Eq. (24), and look for the values of these factors that drive the sail towards the disposal orbit in the minimum time.

## 5. Conclusion

This work has investigated a space debris removal strategy that uses a solar sail to actively dispose of a debris object in low Earth orbit. Locally-optimal control laws have been employed to optimize the sail trajectory, and have proved to be particularly suited and effective in driving the spacecraft towards its target in a highly-perturbed environment where global-optimization techniques would have been challenging to implement.

A blending strategy has been used to control a set of orbital elements at the same time in order to reach the debris' orbit. Despite the fact that the search for optimal weighing factors has required a considerable amount of time, even a low number of generations in the genetic algorithm has provided good solutions for a preliminary design. Besides, the proposed approximate model has not only reduced the computational time, but also provided a good approximation to the more accurate approach.

A future work could include the switching point between 1st and 2nd phases into the optimization process in order to derive the best possible sequence depending on the characteristics of the debris' orbit.

An interesting application of this method could be a multiple debris removal mission, where a single sail can sequentially capture and de-orbit many objects, thus making the use of this propulsion system even more attractive.

## References

[1] D. J. Kessler and B. G. Cour-Palais. Collision frequency of artificial satellites: The creation of a debris belt. *J Geophys Res*, 83 (A6):2637–2646, 1978.

[2] C. Lücking, C. Colombo, and C. R. McInnes. A passive satellite deorbiting strategy for medium earth orbit using solar radiation pressure and the j2 effect. *Acta Astronautica*, 77:197–206, 8 2012. ISSN 00945765. doi: 10.1016/j.actaastro.2012.03.026.

[3] J. P. Carvalho et al. Analysis of the orbital evolution of space debris using a solar sail and natural forces. *Advances in Space Research*, 70:125–143, 7 2022. ISSN 18791948. doi: 10.1016/j.asr.2022.04.014.

[4] C. Colombo et al. Effects of passive de-orbiting through drag and solar sails and electrodynamic tethers on the space debris environment. In *Proceedings of the 69$^{th}$ International Astronautical Congress (IAC)*, 2018.

[5] V. Schaus et al. On the practical exploitation of perturbative effects in low earth orbit for space debris mitigation. *Advances in Space Research*, 63:1979–1991, 4 2019. ISSN 18791948. doi: 10.1016/j.asr.2019.01.020.

[6] G. Schettino, E. M. Alessi, A. Rossi, and G. B. Valsecchi. Exploiting dynamical perturbations for the end-of-life disposal of spacecraft in leo. *Astronomy and Computing*, 27:1–10, 4 2019. ISSN 22131337. doi: 10.1016/j.ascom.2019.02.001.

[7] I. Iakubivskyi et al. Coulomb drag propulsion experiments of estcube-2 and foresail-1. *Acta Astronautica*, 177:771–783, 12 2020. ISSN 00945765. doi: 10.1016/j.actaastro.2019.11.030.

[8] M. M. Pellegrino and D. J. Scheeres. Optimal deployment of solar radiation pressure enhancement devices for space debris mitigation. American Institute of Aeronautics and Astronautics Inc, AIAA, 2018. ISBN 9781624105333. doi: 10.2514/6.2018-2229.

[9] J.C. Liou. A parametric study on using active debris removal for leo environment remediation. *NASA Johnson Space Center*, 4, 2010.

[10] C. Bonnal, J.M. Ruault, and M.C. Desjean. Active debris removal: Recent progress and current trends. *Acta Astronautica*, 85:51–60, 2013. ISSN 0094-5765. doi: https://doi.org/10.1016/j.actaastro.2012.11.009.

[11] N. Bérend and X. Olive. Bi-objective optimization of a multiple-target active debris removal mission. *Acta Astronautica*, 122: 324–335, 2016. ISSN 0094-5765. doi: https://doi.org/10.1016/j.actaastro.2016.02.005.

[12] V. Braun et al. Active debris removal of multiple priority targets. *Advances in Space Research*, 51(9):1638–1648, 2013. ISSN 0273-1177. doi: https://doi.org/10.1016/j.asr.2012.12.003.

[13] G. Viavattene et al. Design of multiple space debris removal missions using machine learning. *Acta Astronautica*, 193:277–286, 4 2022. ISSN 00945765. doi: 10.1016/j.actaastro.2021.12.051.

[14] P. Kelly and R. Bevilacqua. An optimized analytical solution for geostationary debris removal using solar sails. *Acta Astronautica*, 162:72–86, 9 2019. ISSN 00945765. doi: 10.1016/j.actaastro.2019.05.055.

[15] P. Kelly and R. Bevilacqua. Geostationary debris mitigation using minimum time solar sail trajectories with eclipse constraints. *Optimal Control Applications and Methods*, 42:279–304, 1 2021. ISSN 10991514. doi: 10.1002/oca.2676.

[16] M. J. H. Walker, B. Ireland, and J. Owens. A set modified equinoctial orbit elements. *Celestial Mechanics*, 36:409–419, 8 1985. doi: 10.1007/BF01227493.

[17] M. J. H. Walker. A set of modified equinoctial orbit elements. *Celestial Mechanics*, 38:391–392, 1986. doi: 10.1007/BF01238929.

[18] J. T. Betts. *Practical Methods for Optimal Control and Estimation using Nonlinear Programming*. 2010.

[19] C. R. McInnes. Solar sailing technology, dynamics and mission applications, 1999.

[20] L. Carzana, P. Visser, and J. Heiligers. Locally optimal control laws for earth-bound solar sailing with atmospheric drag. *Aerospace Science and Technology*, 127, 8 2022. ISSN 12709638. doi: 10.1016/j.ast.2022.107666.

[21] G. Mengali and A. A. Quarta. Near-optimal solar-sail orbit-raising from low earth orbit. *Journal of Spacecraft and Rockets*, 42:954–958, 2005. ISSN 15336794. doi: 10.2514/1.14184.

[22] J. A. Storch. Aerodynamic disturbances on spacecraft in free-molecular flow. *The Aerospace Corporation*, 2002.

[23] J. Picone, A.E. Hedin, D. Drob, and A. Aikin. Nrlmsise-00 empirical model of the atmosphere: Statistical comparison and scientific issues. *Journal of Geophysical Research*, 107, 12 2002. doi: 10.1029/2002JA009430.

[24] V. Stolbunov, M. Ceriotti, C. Colombo, and C. R. McInnes. Optimal law for inclination change in an atmosphere through solar sailing. *Journal of Guidance, Control, and Dynamics*, 36:1310–1323, 2013. doi: 10.2514/1.59931.

[25] H. D. Curtis. *Orbital Mechanics for Engineering Students*. Elsevier, 2020. doi: 10.1016/b978-0-08-102133-0.09982-7.

[26] M. Macdonald and C. R. McInnes. Analytical control laws for planet-centered solar sailing. *Journal of Guidance, Control, and Dynamics*, 28:1038–1048, 2005. ISSN 15333884. doi: 10.2514/1.11400.

[27] M. Macdonald, C. R. McInnes, and B. Dachwald. Heliocentric solar sail orbit transfers with locally optimal control laws. *Journal of Spacecraft and Rockets*, 44:273–276, 2007. ISSN 15336794. doi: 10.2514/1.17297.

[28] M. Bassetto, A. A. Quarta, and G. Mengali. Locally-optimal electric sail transfer. *Proceedings of the Institution of Mechanical Engineers, Part G: Journal of Aerospace Engineering*, 233:166–179, 1 2019. ISSN 20413025. doi: 10.1177/0954410017728975.

[29] H. J. Holt. *Trajectory Design using Lyapunov Control Laws and Reinforcement Learning*. PhD thesis, University of Surrey, 2023.